# Simultaneous measurements of velocity and scalar fields: application in crossflowing jets and lifted jet diffusion flames

**By L. K. Su AND M. G. Mungal**

## 1. Motivation and objectives

Developments in laser-based imaging diagnostics in recent years have greatly facilitated two-dimensional measurements of velocity and scalar fields in turbulent flows. Particle image velocimetry (PIV) is widely used for velocity field measurements, while such techniques as planar laser-induced fluorescence (PLIF) and planar Rayleigh scattering have been applied in measurements of scalar fields. These two-dimensional methods afford direct access to the structural features of the velocity and scalar fields. This has proven useful in studies which seek to understand the interactions between large and small scale structures in the velocity and velocity gradient fields or in the entrainment and mixing processes. These types of measurements are also valuable as benchmarks for computational methods. This is particularly true for those computational methods which appeal to the tendency towards large-scale organization of turbulence structures such as large eddy simulation (LES).

With the increasing refinement of planar measurement techniques, attention has begun to be given to simultaneous measurement of velocity and scalar fields. Working in a turbulent jet in water, Su & Dahm (1996) obtained results for the gradients of velocity and a conserved scalar through simultaneous application of scalar imaging velocimetry (SIV) and PLIF, and they explored the relationships between the vorticity vector, strain rate tensor, and scalar gradient vector at the small scales. More recently, simultaneous PIV and PLIF of combustion radicals such as OH and CH has been demonstrated (by Rehm & Clemens (1997), Hasselbrink *et al.* (1997), and Carter *et al.* (1998), among others). The PLIF in these cases is used to mark the reaction zones, permitting analyses of velocities and velocity gradients conditioned on flame location, for example.

This paper describes the simultaneous application of PIV and PLIF in two different gas-phase flow systems, the non-reacting turbulent crossflowing jet and the lifted turbulent jet diffusion flame. The fluorescence medium in each case is acetone vapor introduced into the fuel stream so the PLIF fields represent the jet fluid concentration. A similar technique has been applied by Tsurikov *et al.* (1999) to the small scales of a round turbulent jet. The majority of the present discussion concerns the crossflowing turbulent jet, in which a jet is injected into a perpendicular fluid stream. This flow is of considerable significance in combustion applications, ranging from aeropropulsion to gas-burning power generation to the on-site purging of excess gases at oil drilling sites. Despite the abundance of engineering applications, however, the body of research devoted to mixing in the crossflowing jet is

small. Among other issues, the complicated vortical structure of the crossflowing jet (e.g. Fric & Roshko, 1994) makes theoretical treatment difficult. A problem common to modeling work is the difficulty in modeling the near field of the flow. Additionally, experimental evidence suggests that the flow is very sensitive to the ratio of jet velocity to crossflow velocity, which constrains efforts to make general conclusions about the flow configuration. The present measurements are intended to provide a comprehensive view of the velocity and conserved scalar fields in the developing region of the flow. All measurements are made at a single jet-to-crossflow velocity ratio ($r = 5.7$). The effect of the crossflow velocity profile is considered by placing the jet exit nozzle both flush with the wind tunnel wall and also outside the crossflow boundary layer. Velocity ratios of around 5 are of particular interest in aerospace propulsion applications. By performing the planar measurements in the center plane (i.e. the jet symmetry plane) and at various positions off the center plane, we are able to evaluate the three-dimensionality of the flow. These results are also of direct interest to ongoing efforts to compute mixing and combustion in the crossflowing jet (e.g. Schlüter *et al.,* 1999).

The second flow to which the simultaneous PIV/acetone PLIF technique is applied is a lifted jet diffusion flame. The mechanism by which such a flame stabilizes has been the subject of much debate. Theories variously describe the base of a lifted jet diffusion flame as an ensemble of laminar diffusion flamelets which can be quenched by high scalar dissipation rates (Peters & Williams, 1983), as a partially premixed 'triple' flame (Dold, 1988), or as combining elements of both (Müller *et al.,* 1994). Muñiz & Mungal (1997) applied PIV to the base of a lifted jet diffusion flame to determine flame stabilization velocities. The technique applied there, however, did not conclusively isolate the true flame base, nor were mixture fraction measurements made. Watson *et al.,* (1999) performed CH/OH PLIF and PIV simultaneously at the flame base, and while the identification of the flame base in those measurements is more conclusive, mixture fraction data were also not available. The present measurements augment these prior studies by providing a complete picture of the local velocity and mixture fraction fields at the flame base, allowing clarification of the relative importance of premixed flame propagation and diffusion flame quenching in the flame stabilization process.

## 2. Accomplishments

### *2.1 Diagnostic method*

This section provides a brief discussion of the laser diagnostic techniques used in these experiments. Additional details may be found in Su *et al.* (2000). Both the nonreacting crossflowing jet and the lifted jet diffusion flame use substantially the same optical arrangement.

To provide the Mie scattering signal for particle image velocimetry, the flows are seeded with either submicron aluminum oxide particles or a glycerol-water fog. A single, dual cavity Nd:YAG laser (with 532 nm output) is used to produce two laser sheet pulses in quick succession. The time delay between pulses is as short as 8 $\mu$s. The resulting scattering signal is collected by an interline transfer CCD camera.
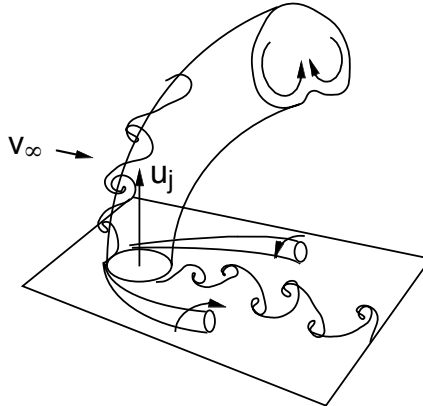
FIGURE 1.    The vortical structure of the crossflowing jet.

The frame transfer capability of this camera allows each of the two closely spaced laser sheet pulses to be captured in a separate image. This permits the use of a cross-correlation PIV algorithm (Hasselbrink, 1999), which eliminates directional ambiguity and yields improved resolution over single-image autocorrelation techniques. The algorithm used here also incorporates iterative interrogation window offset to increase vector yield.

For the laser-induced fluorescence, acetone is seeded into the jet fluid stream to approximately 10% by volume. To excite the fluorescence signal, a XeCl excimer laser with 308 nm output is used. The PLIF signal is captured by a low-noise, high-sensitivity CCD camera. Optical filters separate the PLIF signal (which peaks in the range 400-500 nm) from the much brighter Mie scattering signal at 532 nm. Post-processing of the PLIF data corrects for background light levels, non-uniformity in laser sheet intensity, and local laser intensity attenuation caused by passage of the sheet through the fluorescent medium.

Prior to entering the measurement area, both the 532 nm and 308 nm laser beams are passed through a focusing spherical lens, a diverging cylindrical lens to form the sheets, and a converging cylindrical lens to control the sheet spreading angle. Special care is taken to ensure that the two laser sheets are spatially coincident throughout the measurement area. The centers of the two sheets are separated by no more than 50 $\mu$m throughout the measurement area, where the thickness of the 532 nm sheet varies from approximately 300 to 800 $\mu$m, and the thickness of the 308 nm sheet ranges from 500 to 1000 $\mu$m.

### 2.2 Crossflowing turbulent jet

A schematic of the characteristic vortical structures of the crossflowing jet is given in Fig. 1. Shown are the horseshoe vortices which form at the upstream side of the jet exit, the jet shear layer instability on the jet windward surface, the wake vortices, and the counter-rotating vortex pair (CVP). The CVP becomes the dominant structural feature of the crossflowing jet as the flow develops and is responsible for much of the difficulty in modeling the flow.

In analyzing the scaling properties of the crossflowing jet, the flow may be divided

into three regimes. In the near field, for sufficiently large velocity ratio $r \equiv u_j/v_\infty$, the jet momentum dominates and the flow can be expected to approximate a pure jet. The flow then bends through an intermediate region until, in the very far field, memory of the initial conditions will be lost and the flow is expected to resemble a wake. However, whether the flow does attain this asymptotic state, and whether it displays self-similarity, are still unclear. The answers may depend, for example, on if the nozzle exit is flush with a wall as shown in Fig. 1, or if the exit is well away from any flow boundaries.

### 2.2.1 Flow conditions

These experiments are performed in an updraft wind tunnel with air as both jet fluid and crossflow fluid. For the Mie scattering for PIV, the jet fluid is seeded with aluminum oxide particles (in addition to the acetone seeding for PLIF), and the coflow is seeded with a glycerol-water fog. The maximum crossflow velocity in the tunnel is $v_\infty = 2.95$ m/s. The jet nozzle is a simple pipe with 6.35 mm outer diameter, inner diameter $d = 4.53$ mm, and a length of 320 mm. In the absence of a crossflow, fully developed pipe flow conditions would prevail at the jet exit; the presence of the crossflow, however, is known to affect the jet exit profile (e.g. Yuan, 1997). The average (bulk) jet velocity based on volumetric flow rate is 16.9 m/s, giving a velocity ratio of 5.7 and a jet exit Reynolds number of 5000.

The planar measurement area extends from the jet exit and encompasses the onset of the region identified as the far field by Smith & Mungal (1998) on the basis of scalar measurements. To permit assessment of the effect of the crossflow boundary layer on the flow development, two jet nozzle positions are considered, the first in which the nozzle exit is flush with the wind tunnel wall, and the second in which the nozzle protrudes 100 mm into the crossflow. The 80% point of the boundary layer profile lies 6 mm from the wind tunnel wall, so in this protruding nozzle case the jet is well outside of the crossflow boundary layer. To evaluate the three-dimensionality of the flow, the planar measurements are taken in the jet center plane as well as in planes located at 0.22, 0.45, 0.67, 0.89, and 1.11 $rd$ off of the center plane. The parameter $rd$ is used because it has been shown in other studies that flow trajectories, jet widths, etc. for different $r$ values are in good agreement when distances are normalized by $rd$.

A sample PLIF image, taken in the center plane with the protruding nozzle, is shown in Fig. 2*a*. Here $x$ is the initial jet direction, $y$ is the crossflow direction, and $z$ is out-of-plane. In these measurements it is necessary to include the jet potential core in the imaging region in order to permit the correlation of measured signal levels with jet fluid concentration. The size of the imaging region is then restricted by the desire to resolve fine-scale fluctuations in the scalar field in the 512 x 512 pixel images. The resulting raw PLIF images span roughly 3.5 $rd$ per side. In contrast, it is not required that the PIV images include the potential core for reference purposes. The PIV processing, however, inherently compromises resolution, yielding here a final vector resolution of 100 x 100 pixels from the original 1k x 1k Mie scattering images. In order that the processed PIV results resolve fluctuations in the velocity field, the full PLIF imaging region is tiled by eight smaller PIV imaging windows
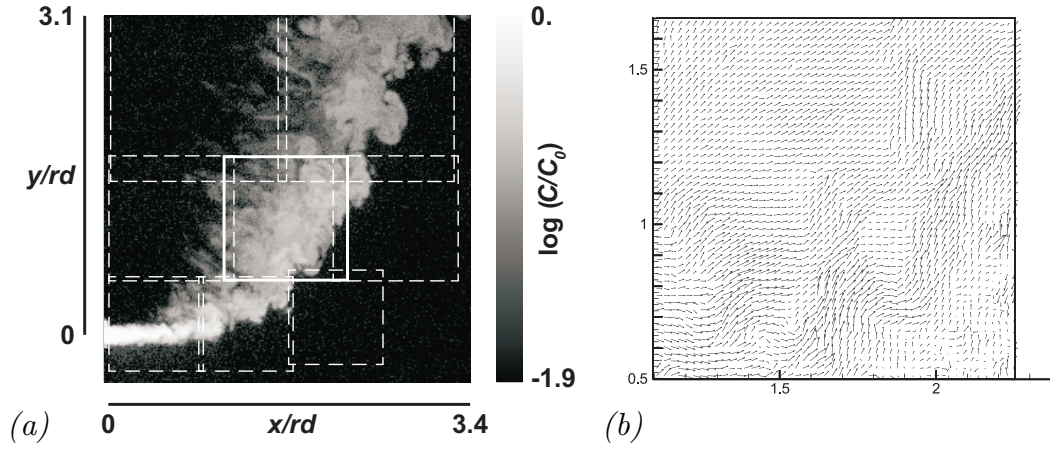
FIGURE 2. A sample image pair, from the center plane of the protruding nozzle case. *(a)* The scalar field, showing the 8 imaging subwindows used for PIV. *(b)* The PIV vector field corresponding to the solid window in *(a)*.
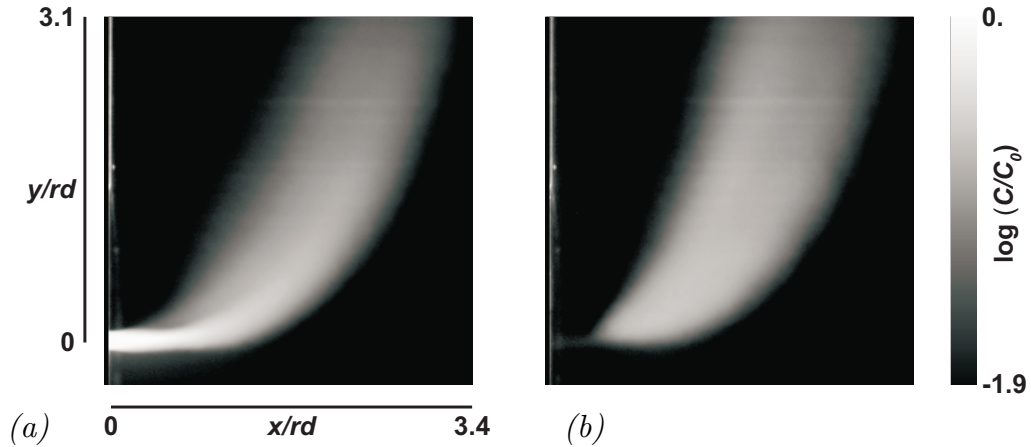


FIGURE 3. Averaged scalar field for the flush nozzle case, in *(a)* the jet center plane, and in *(b)* the plane $z = 0.22 \ rd$. Values are normalized by the initial jet concentration $C_0$.

as indicated by the dashed boxes in Fig. 2*a*. For the particular scalar field shown in the figure, the simultaneous PIV field is given in Fig. 2*b* and corresponds to the solid box in 2*a*.

### 2.2.2 Mean scalar field structure and scaling

The averaged scalar field from the center plane, for the flush nozzle case, is given in Fig. 3*a*. Figure 3*b* shows the averaged scalar field for the plane $z = 0.22 \ rd$. The averages are compiled over 855 and 634 images, respectively. Figure 4 shows the jet development in terms of the trajectory of the points of maximum scalar concentration in the center plane for both the flush and protruding nozzle cases. This trajectory will be termed the centerline in the following discussion. The figure shows the tendency of the jet issuing from the flush nozzle to impinge further into
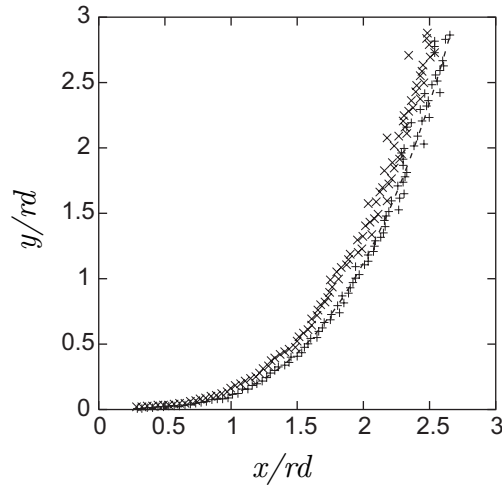
FIGURE 4. Scalar centerline trajectories. $+$, flush nozzle. $\times$, protruding nozzle. $----$ , fit to flush nozzle data of Eq. 1.
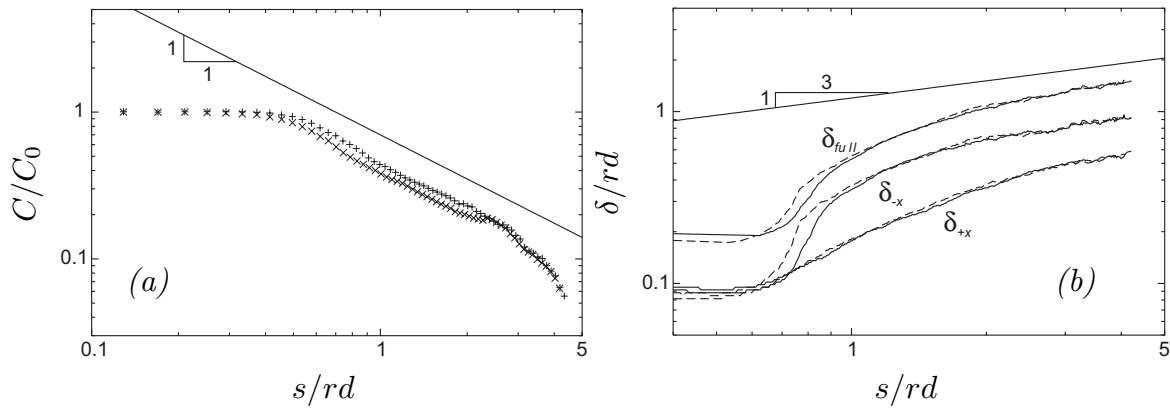


FIGURE 5. *(a)* Decay of maximum scalar concentration with downstream distance in the center plane. $+$, flush nozzle. $\times$, protruding nozzle. *(b)* Scalar flow widths in the center plane. ——— , the flush nozzle case. $----$ , the protruding nozzle case.

the crossflow. The dashed line is a least-squares fit to the flush nozzle data of the function

$$(x/rd) = A(y/rd)^m, \tag{1}$$

with A = 1.95 and m = 0.302. The fit to the protruding nozzle data gives A = 1.81 and m = 0.323. The tendency of the flow in the flush nozzle case to penetrate further into the crossflow can be intuitively explained by noting that, in that case, the jet initially flows through low-momentum fluid in the crossflow boundary layer. The analysis of velocity field trajectories suggests that the picture may be more complex, however (Section 2.2.3).

The decay of the maximum scalar concentration for both the flush and protruding nozzle cases is shown in Fig. 5a. The data are plotted in terms of the centerline downstream coordinate, $s$, which is determined through numerical integration of the best-fit trajectories defined by Eq. 1. Beyond the potential core, the maximum

concentration $C(s)$ decays roughly as $1/s$, which is the decay dependence seen in simple jets. This contrasts with the results of Smith & Mungal (1998), for values of $r$ ranging from 5 to 25, who found an initial decay faster than $1/s$. The results of Smith & Mungal also showed distinct branch points where the concentration decay abruptly slowed, possibly to an $s^{-2/3}$ dependence which would indicate wake-like behavior. However, the present data show a decay rate which actually increases beyond $s/rd \approx 2.5$. Also of interest is the agreement between the flush and protruding nozzle cases when the data are plotted in this centerline coordinate. The functional dependencies of the decay curves are similar, as is the point at which the decay rate increases beyond $1/s$, though the potential core in the flush nozzle case penetrates further into $s$ space.

Figure 5$b$ shows the dependence of the flow widths on the centerline coordinate $s$. The flow nominal half-width for a given $s$ is computed by first determining the maximum concentration, $C(s)$, then moving in the trajectory normal direction until the concentration drops to a specified fraction (here, 20%) of $C(s)$. Because the flow is not symmetric about the centerline trajectory in the imaging plane, it is necessary to compute these partial widths separately for both the $-x$ direction (i.e. towards the wake region) and the $+x$ direction (towards the jet outer edge). We denote these partial widths by $\delta_{-x}$ and $\delta_{+x}$ and the full width by $\delta_{full} \equiv \delta_{-x} + \delta_{+x}$. Figure 5$b$ shows the results for $\delta_{-x}$, $\delta_{+x}$, and $\delta_{full}$ as functions of $s$. The lack of symmetry, with $\delta_{-x} > \delta_{+x}$, is clear. This asymmetry is due to jet fluid which is stripped away from the developing region of the jet by the crossflow and is deposited in the wake region. Just outside of the potential core, $\delta_{full}$ grows much faster than $s$, the pure jet growth rate. For higher values of $s$, the $\delta_{full}$ curve shows evidence of an asymptotic approach to an $s^{1/3}$ dependence, which would correspond to a wake-like scaling. Finally, the curves for both the flush and protruding nozzle cases are in good agreement for $s/rd > 1$, again showing the similarity in flow development for the two configurations when the centerline coordinate $s$ is used.

Interestingly, while the flow width, $\delta_{full}$, appears for both the flush and protruding nozzle cases to be approaching a dependence on the centerline coordinate, $s$, consistent with a wake-like scaling, the concentration decay does not. These scaling laws rely upon self-similarity in the mean profiles, so it is reasonable to look to a lack of self-similarity to explain the departures from wake scaling seen in the data. The three-dimensionality of the flow will also be important. Figure 6$a$ shows the maximum scalar concentration as a function of $s$ for the jet center plane as well as for planes located 0.22, 0.45, 0.67, and 0.89 $rd$ off of the center plane. The data are for the flush nozzle case; the protruding nozzle data are qualitatively similar. The coordinate $s$ for all of these curves is determined from the jet centerline trajectory in the center plane, and the maximum scalar values are those in the in-plane normal direction to that trajectory. Of particular note in the figure is that the highest scalar concentration is not found in the center plane for $s/rd < 2.2$. Instead, the jet cross-section appears to take on a bimodal profile in which the scalar maxima lie off of the center plane. This is sufficient to explain the deviation from a wake-like concentration decay in the center plane because the wake similarity profile has its
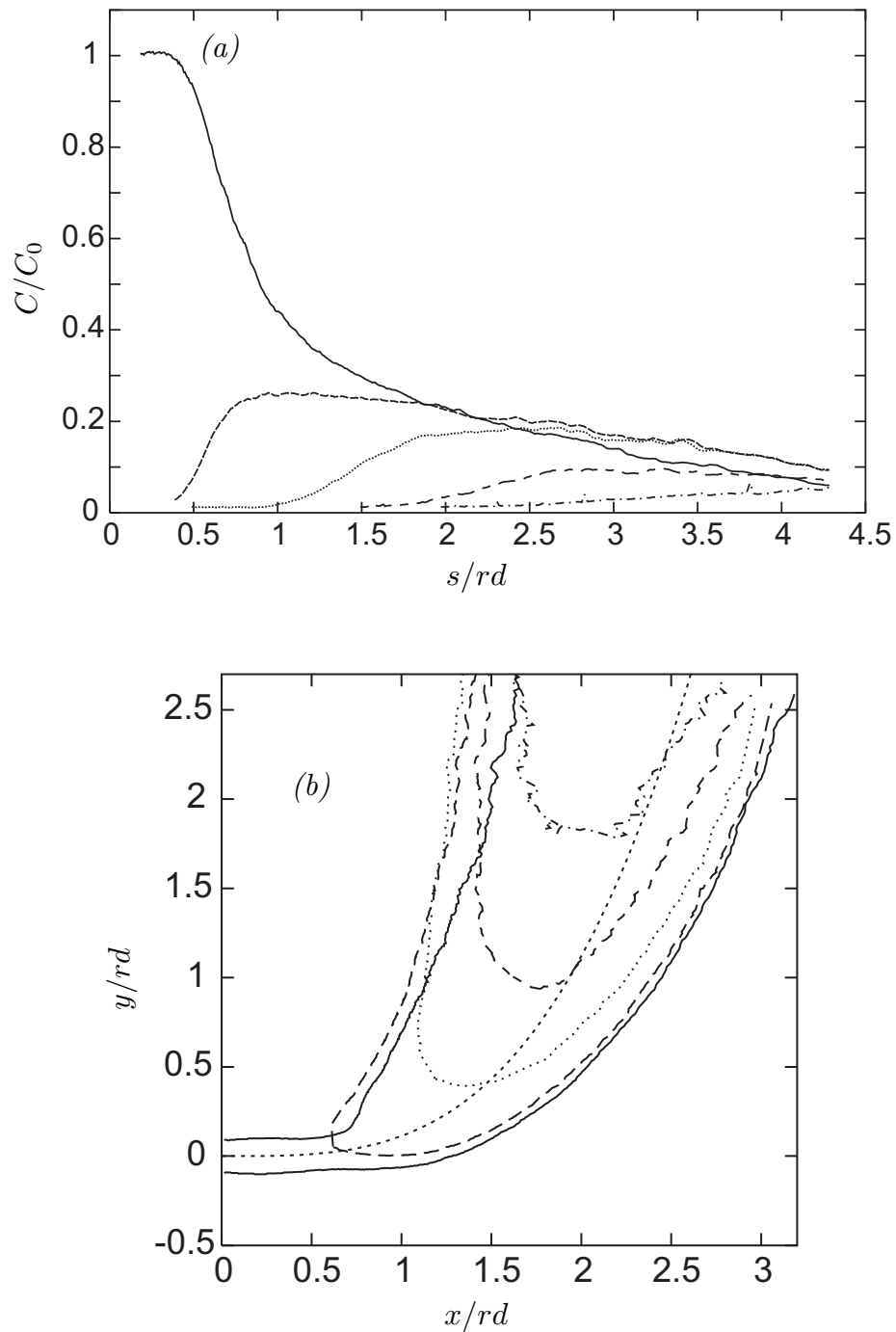
FIGURE 6. Three-dimensionality in the scalar field. *(a)* Decay of maximum scalar concentration with downstream distance, for the flush nozzle case. *(b)* Boundary contours for the scalar field. ——— , the center plane. ---- , the $z = 0.22\ rd$ plane. ········· , $z = 0.45\ rd$. ——— , $z = 0.67\ rd$. —·— , $z = 0.89\ rd$.
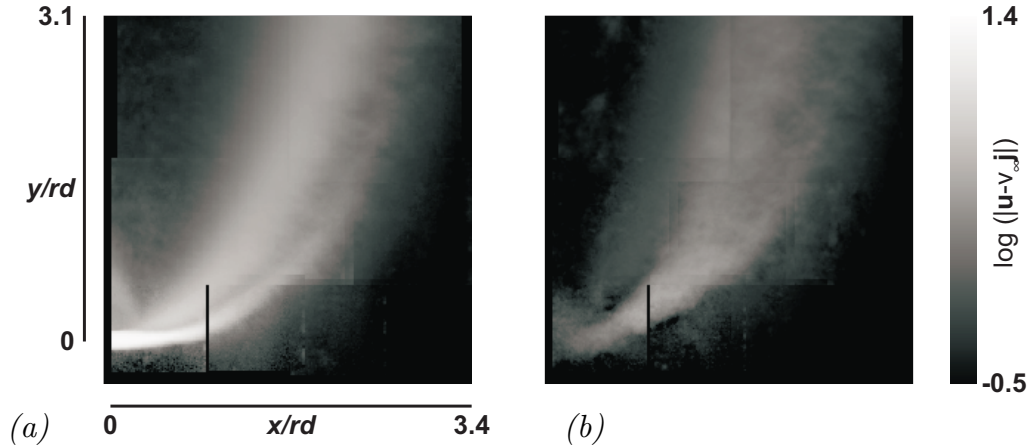
FIGURE 7. Averaged velocity magnitude field for the protruding nozzle case, with the crossflow speed $v_\infty$ subtracted from the vertical component. *(a)* The field in the jet center plane, and in *(b)* the plane $z = 0.22\ rd$. Velocity values have units m/s.

peak on the centerline.

Figure 6*b* presents a different view of the three-dimensionality of the scalar field. Shown are the boundary contours for the scalar field in the center plane and in the planes $z = 0.22, 0.45, 0.67$, and $0.89\ rd$, together with the centerline trajectory for the center plane. The contours represent the loci of points in a given trajectory-normal plane where the local scalar value is 20% of the maximum scalar value in the center plane. On the outer boundary of the flow (i.e. the positive $x$ side of the centerline), the deepest penetration occurs in the center plane with progressively shallower penetration for increasing off-center position $z$. Meanwhile, on the wake side of the flow, with increasing $y$ the boundaries for the off-center planes all lie further from the centerline trajectory than does the boundary in the center plane. This corresponds to a 'kidney'-like shape of the flow cross-section as depicted in Fig. 1. This cross-sectional shape arises because of the dominant role played by the counter-rotating vortex pair (CVP) in the large-scale organization of the flow.

It is instructive that the current measurements show good agreement in decay rates and flow widths (when expressed in terms of $s$) between the flush and protruding nozzle cases, yet the decay rates differ from those reported by Smith & Mungal, whose results were consistent over a range of velocity ratios $r$. The most notable difference is that Smith & Mungal used a top-hat jet exit velocity profile while the present data use a pipe flow profile. The conclusion drawn here is that the jet exit profile plays a larger role in establishing the scaling properties of the mixing field than does the jet nozzle position or the value of $r$.

*2.2.3 Mean velocity field structure and scaling*

Figure 7 shows the averaged velocity magnitude fields for the protruding nozzle case both in the jet center plane and in the plane $z = 0.22\ rd$. As mentioned above, these full fields are composed of eight sub-windows. For each sub-window in the
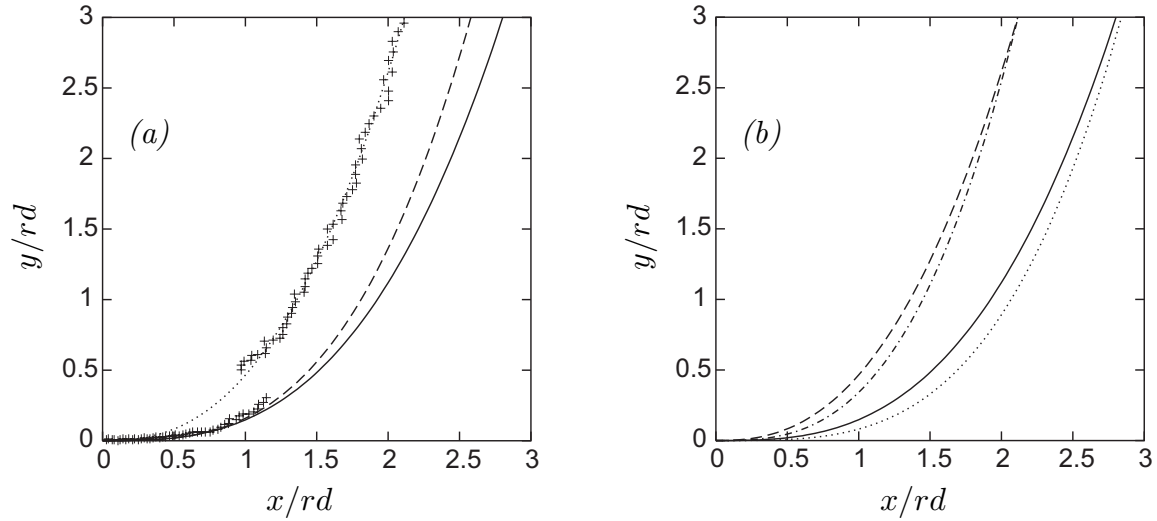
FIGURE 8. Trajectories of the velocity field in the center plane. *(a)* Bifurcated structure of the local maxima in the velocity magnitude field. Data from the protruding nozzle case. +, local maxima of $|\mathbf{u}-v_\infty\hat{\mathbf{j}}|$. ——— , center streamline. - - - - , scalar centerline trajectory. ········ , fit of Eq. 1 to the wake portion of the $|\mathbf{u}-v_\infty\hat{\mathbf{j}}|$ trajectory. *(b)* Comparison of the protruding and flush nozzle positions. For the protruding nozzle: ——— , center streamline. - - - - , wake trajectory. For the flush nozzle: ········ , center streamline. —·— , wake trajectory.

center plane, between 98 and 145 images were averaged. Between 67 and 92 images were averaged in each sub-window in the $z = 0.22\ rd$ plane. The crossflow speed, $v_\infty$, has been subtracted from the vertical velocity component in these figures. In Fig. 7*a* it is apparent that the region of large velocity magnitudes has a bifurcated structure, with one branch appearing to evolve from the initial jet trajectory while the other branch turns more sharply into the wake region of the jet. The averaged velocity fields for the flush nozzle case show the same qualitative behavior. This contrasts with the averaged scalar field of Fig. 3*a*, in which the highest values follow a single trajectory.

The bifurcated structure is shown clearly in Fig. 8*a*, which shows the trajectory of the points of maximum velocity magnitude for the protruding nozzle case (again, with the crossflow speed subtracted from the vertical velocity component). The 'center streamline' plotted in the figure is found by performing a ray tracing from the center of the nozzle exit through the averaged velocity field. A fourth-order Runge-Kutta integration is used. The points of maximum velocity magnitude initially follow this center streamline quite closely. In the notation of Eq. 1, the fit to the center streamline has A = 1.92 and m = 0.342. Notably, the center streamline lies to the outside (the windward side) of the scalar centerline trajectory. At roughly $s = 1.3$ (measured along the center streamline), the points of maximum velocity magnitude abruptly shift to a trajectory lying in the wake region of the flow. The fit to this wake trajectory has A = 1.36 and m = 0.402. Figure 8*b* compares the center streamline and wake trajectories for the protruding and flush nozzle
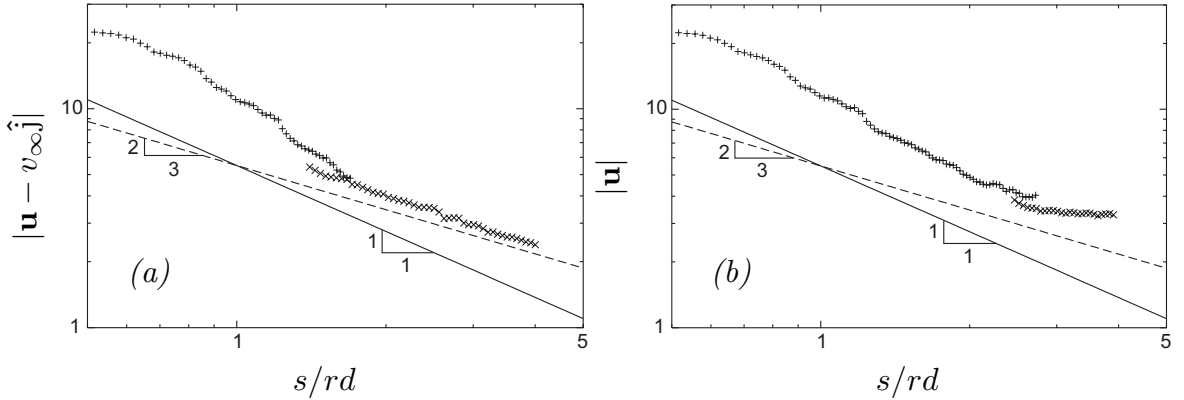
FIGURE 9.    Decay of maximum velocity magnitude with downstream distance in the center plane for the flush nozzle case. *(a)* Magnitude computed with crossflow speed subtracted, showing possible approach to wake scaling. *(b)* Raw velocity magnitude.

cases, demonstrating again that the flow penetrates further into the crossflow with the nozzle exit placed flush with the facility wall. Whether this trend persists into the far-field, however, is somewhat in question. At the upper boundary of the measurement area ($y \approx 3\,rd$), the wake trajectory for the protruding nozzle case appears to be crossing to the outside of the trajectory for the flush nozzle. Similarly, the center streamline for the protruding nozzle case draws closer to the center streamline for the flush case for increasing downstream distance. As pointed out by Schlüter *et al.* (1999), for example, the low pressure region in the wake of the jet has a strong effect on the jet trajectory. It is possible that while the jet issuing from the flush nozzle initially penetrates further into the flow because of the lower crossflow momentum in the boundary layer, the presence of the wall results in a stronger low pressure region which acts to draw the flow back toward the wall as the flow moves downstream. Clarification of this point may require pressure measurements in the wake region.

As discussed above, the crossflowing jet can be viewed as approximating a pure jet in its near field and a wake in its far field. In attempting to identify these scalings, the choice of appropriate variables is important. For the near field, the jet is well described by the raw velocity magnitude $|\mathbf{u}|$. However, because wake scaling is defined in terms of the deficit velocity, the appropriate variable for the crossflowing jet far field is the magnitude of the velocity with the crossflow speed subtracted as shown in Fig. 7. In Fig. 9$a$, the decay of this $|\mathbf{u} - v_\infty \hat{\mathbf{j}}|$ term is plotted against the downstream coordinate $s$, for the flush nozzle case (the protruding nozzle case is qualitatively similar). The two decay curves represent the initial trajectory and later wake trajectory; the curves do not join smoothly because $s$ is computed separately for each curve based the individual fits to Eq. 1. Also plotted in the figure are curves with slope -1 and -2/3. In the initial portion of the trajectory, and outside of the potential core, the magnitude decays faster than $1/s$, the pure jet rate, and does not appear to follow a power law scaling. In the wake portion of the

trajectory, the magnitude appears to adhere to a power law decay with dependence very close to $s^{-2/3}$, suggesting a wake-like scaling. Figure 9$b$ shows the raw velocity magnitude $|\mathbf{u}|$ as a function of $s$. In this figure the magnitude along the initial trajectory shows some evidence of following a jet-like decay $1/s$, while magnitude in the wake trajectory shows no power law dependence, instead asymptotically approaching the crossflow velocity $v_\infty = 2.95$ m/s. This emphasizes that the raw velocity magnitude $|\mathbf{u}|$ is the appropriate variable for revealing the possible jet-like scaling of velocity magnitude decay in the near field, while the crossflow-subtracted magnitude $|\mathbf{u} - v_\infty\hat{\mathbf{j}}|$ is the proper variable for describing the possible wake-like scaling in the far field.

The flow width of the $|\mathbf{u} - v_\infty\hat{\mathbf{j}}|$ field for both the protruding and flush nozzles is shown in Fig. 10$a$. Plotted are the full flow widths $\delta_{full}$, defined as before as the distance between points, in the trajectory-normal direction, where the magnitude is 20% of the maximum value. As with the scalar growth rates shown in Fig. 5$b$, the initial growth rate exceeds the linear dependence of a pure jet. In Fig. 10$a$, there is then an abrupt transition to a slower growth rate which is very close to the wake growth rate $s^{1/3}$. The curves for the flush and protruding nozzle cases are very similar, including the positions of the transition points, again pointing out the similarity in the flow scalings when expressed in terms of $s$.

The boundary contours for the $|\mathbf{u} - v_\infty\hat{\mathbf{j}}|$ field in the center plane and in the planes $z = 0.22$, 0.45, and 0.67 $rd$ for the flush nozzle case are shown in Fig. 10$b$. The boundary contours are defined as in Fig. 6$b$. Also plotted in Fig. 10$b$ is the center streamline. The region enclosed by each contour is heavily weighted toward the $-x$ side of the center streamline, indicating the dominance of the wake region in the flow development. Interestingly, the kidney-shaped flow cross-section described by the scalar contours in Fig. 6$b$ is not duplicated here. Instead, the velocity magnitude contours for the planes with higher $z$ are contained within the contours for lower $z$, indicating that the cross-sectional contours of velocity magnitude are everywhere convex in shape. The absence of the out-of-plane velocity component perhaps explains the departure from the kidney-shaped cross-section. (The averaged out-of-plane velocity component in the center plane of the jet is identically zero by symmetry, and thus its absence does not affect the results shown in Figs. 8-10$a$.)

### 2.2.4 Fluctuation quantities

Turbulence quantities involving the fluctuating velocity and scalar field terms are available due to the high resolution of the present data. In particular, the simultaneous nature of the measurements permits the scalar flux components, $\overline{u'C'}$ and $\overline{v'C'}$, to be determined. From the evidence of previous computations, these scalar flux terms are very difficult to compute accurately (Alvarez *et al.*, 1993).

Figure 11 shows profiles of the scalar flux components $\overline{u'C'}$ and $\overline{v'C'}$ in the center plane for the protruding nozzle case. Profiles are shown for $y = 0.5$, 1.0, 1.5, and 2.5 $rd$. The center streamline and wake trajectory positions for each $y$ position are indicated. The present data agree with the heat flux profiles reported by Andreopoulos (1983) in showing a negative correlation between $\overline{u'C'}$ and $\overline{v'C'}$ and in showing that the largest $\overline{u'C'}$ values lie on the outer edge of the jet (larger $x$ values). The present
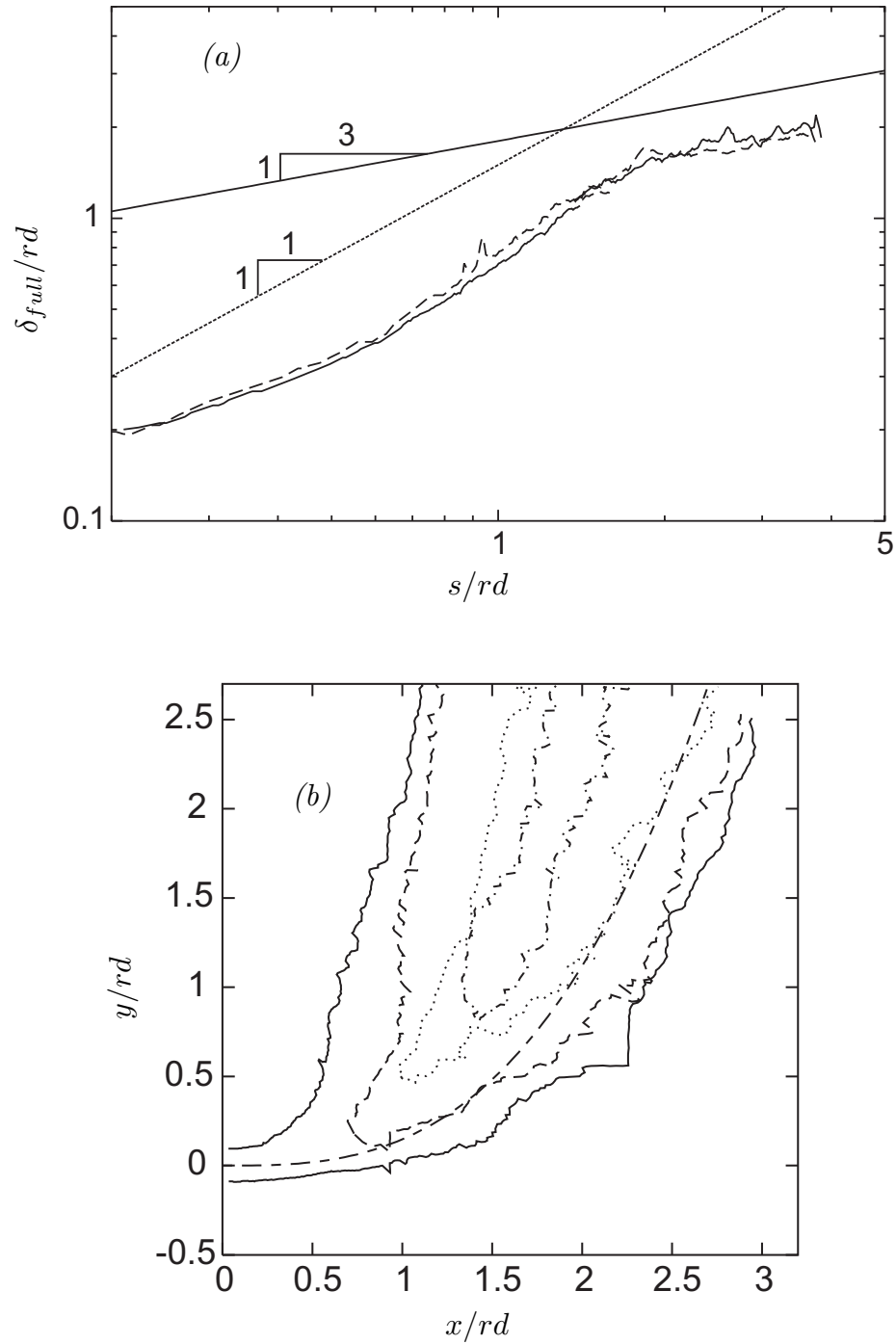
FIGURE 10.  *(a)* Downstream evolution of the flow width of the $|\mathbf{u} - v_\infty \hat{\mathbf{j}}|$ field. ———— , flush nozzle. ---- , protruding nozzle.  *(b)* Boundary contours for the $|\mathbf{u} - v_\infty \hat{\mathbf{j}}|$ field, for the protruding nozzle case. ———— , the center plane. ---- , $z = 0.22\ rd$. ······· , $z = 0.45\ rd$. —·— , $z = 0.67\ rd$.
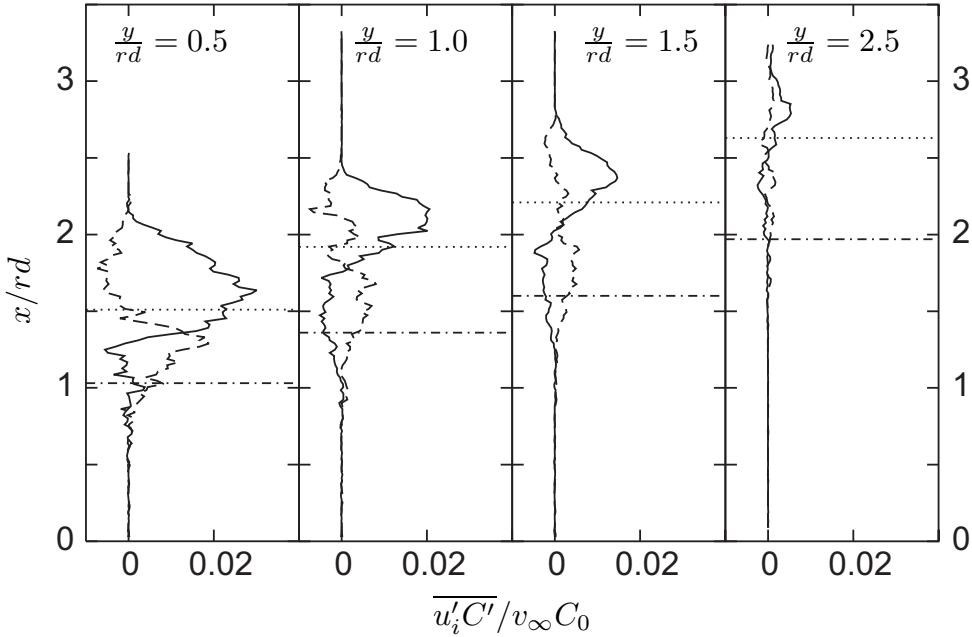
FIGURE 11. Scalar flux profiles in the center plane, for the protruding nozzle case. Results at $y = 0.5$, 1.0, 1.5 and 2.5 $rd$. ——— , the $\overline{u'C'}$ component. ---- , $\overline{v'C'}$. ······· , the center streamline position. —·— , the wake trajectory position.

data differ, however, in showing distinct sign changes in the profiles and in showing magnitudes of $\overline{u'C'}$, which are noticeably larger than the magnitudes of $\overline{v'C'}$. It should be noted that the data of Andreopoulos are for a flow with very low velocity ratio $r = 0.5$, which may be sufficient to explain the discrepancies. This notion is supported by the large-eddy simulations of Yuan (1997) at a velocity ratio, $r = 3.3$, closer to that of the present measurements. Yuan reported $\overline{u'C'}$ profiles which show sign changes similar to those in Fig. 11. Further analysis of these scalar fluxes and other fluctuation quantities can be found in Su *et al.* (2000).

### 2.3 Lifted jet diffusion flame

The base of a lifted, round jet diffusion flame is depicted schematically in Fig. 12. The flame base shows a characteristic annular structure where the high-temperature region surrounds the central fuel jet (in these experiments the fuel is methane). Further downstream in the flow the annulus closes, and the flame surface spans the jet centerline. The present measurements aim to identify the true flame surface and determine the role of velocities and strain rates, and mixture fraction and scalar dissipation, in stabilizing the flame.

The diagnostic technique is substantially similar to that used in the crossflowing jet. However, signal interpretation is complicated somewhat by the presence of the high flame temperatures. In these experiments only the coflow air is seeded for Mie scattering. Separate sets of measurements were made with either aluminum oxide particles or the glycerol-water fog as the seeding medium. The aluminum oxide particles are able to survive the flame temperatures (which are on the order of 2000K), while the glycerol-water particles evaporate at roughly 400K. This property
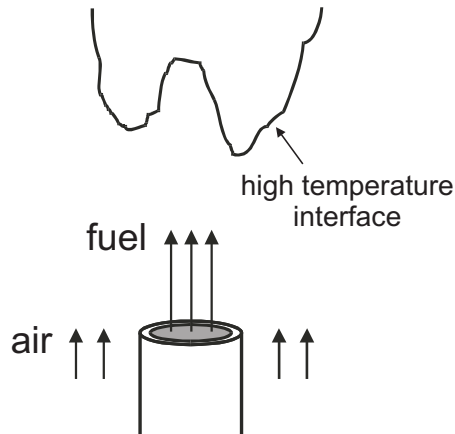
FIGURE 12.   Schematic of the lifted jet diffusion flame.

can be exploited to delineate the interface between high and low temperature fluid at the flame base. When the glycerol-water fog is used for seeding, the Mie scattering images show an abrupt transition to no signal across the high temperature interfaces. The disadvantage of this seeding method is that velocities within the high temperature regions cannot be found. When the aluminum oxide particles are used, the high temperature interfaces are marked by the reduction in the density of Mie scattering particles, owing to the reduction in fluid density. In comparison with fog seeding, the aluminum oxide seeding renders the identification of the high temperature interfaces more uncertain but has the advantage of permitting velocity vector determination within the high temperature regions.

Interpretation of the acetone PLIF signal will also be dependent on temperature. Thurber (1999) considered changes in fluid density, fluorescence yield, and absorption cross-section and showed that the fluorescence signal at 1000K had dropped to roughly 40% of its room temperature value at atmospheric pressure and with 308 nm excitation. At 400K, above which there is no Mie scattering signal from fog particles, the fluorescence signal is roughly 85% of its room temperature value. The PLIF will therefore provide a reasonably accurate measure of fuel concentration at the high-temperature interfaces found from the fog Mie scattering images.

Figure 13 presents sample results from the lifted methane flame. The coflow is seeded with the glycerol-water fog in this case. The jet Reynolds number is roughly 4000, and the coflow speed is approximately equal to the laminar flame speed of methane (roughly 40 cm/s). The fuel concentration field is shown in Fig. 13*a*. The subwindow shown represents the PIV imaging area, and the indicated contour is the high temperature interface determined from the Mie scattering image given in Fig. 13*b*. The drop in Mie scattering signal across the high temperature interface is very evident in Fig. 13*b*. The PIV vector field is shown in Fig. 13*c*. Inspection of the fuel concentration field shows that no fuel is present at the base of the high temperature branch on either side of the jet centerline. This is significant because previous PIV studies, lacking data on the concentration of fuel or combustion radicals, have identified the most upstream portions of the high temperature branches
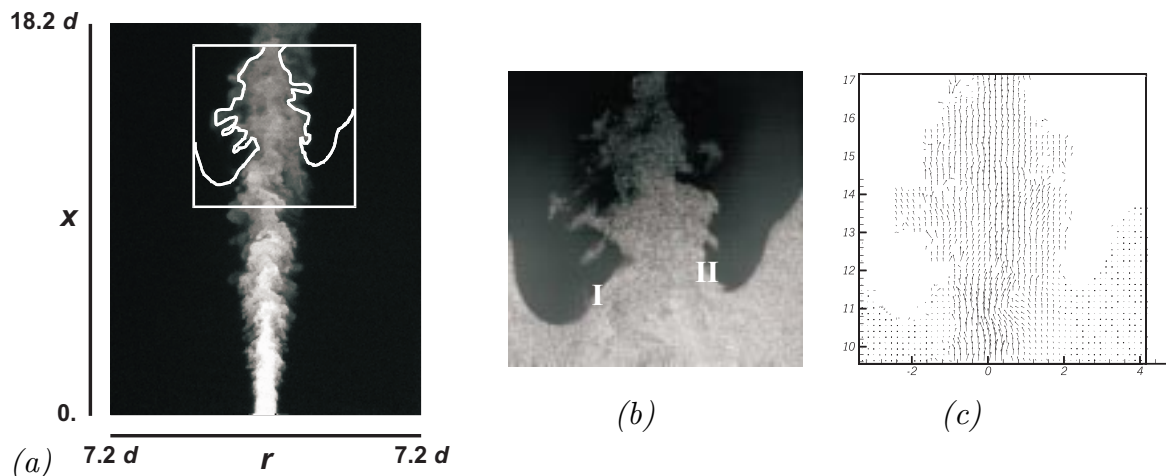
FIGURE 13. Sample PIV/PLIF results for the lifted jet diffusion flame. *(a)* Fuel concentration field from PLIF, with the high temperature interface determined from *(b)* the Mie scattering image, with coflow seeding only. *(c)* PIV velocity vector field.

as the local flame base. The present data suggest instead that the flame lies on the inner edges of the high temperature regions (for example, in the areas labeled I and II in Fig. 13*b*), with the high temperature products propagating radially outward and axially upstream. This view is supported by the recent simultaneous OH/CH PLIF measurements in lifted flames by Watson *et al.* (1999). CH is a short-lived combustion intermediate and is a good marker of the reaction zone, while OH is generated in the reaction zone but persists in regions of high temperature combustion products. The data of Watson *et al.* show narrow CH zones located on the inner edges of broader regions of OH. The high temperature regions as marked by OH are also seen to extend upstream of the CH zones, consistent with Fig. 13.

## 3. Future plans

For the crossflowing turbulent jet, analysis of the structure and scaling of the velocity and scalar fields is virtually complete. Current work includes analysis of the mean vorticity, aiming to determine the role played by the vorticity in the transition from near to far field properties in the flow. The present two-dimensional measurements yield only a limited view of the vorticity dynamics, however, because the vorticity field is dominated by three-dimensional structures. The remainder of current efforts in this flow concern analyses of small scale fluctuations (Section 2.2.4) and small scale gradients, with particular attention paid to the interactions between the scalar and velocity fields. It is hoped that the results will serve as benchmark data for future simulations of crossflowing jets at similar velocity ratios.

Analysis of the lifted jet diffusion flame data is underway. Initial inspection of the simultaneous PIV/PLIF data places the reaction zone on the inner surfaces of the high temperature regions seen at the flame base, consistent with reported simultaneous CH/OH PLIF measurements. With the knowledge of the instantaneous reaction zone position, conditional statistics of velocities, velocity gradients,

and scalar dissipation can be compiled. These statistics will be used to evaluate the relative importance of premixed flame propagation and diffusion flame quenching in the flame stabilization process.

## REFERENCES

ALVAREZ, J., JONES, W. P. & SEOUD, R. 1993 Predictions of momentum and scalar fields in a jet in cross-flow using first and second order turbulence closures. In *Computational and Experimental Assessment of Jets in Cross Flow, AGARD CP-534*, 24-1–24-10.

ANDREOPOULOS, J. 1983 Heat transfer measurements in a heated jet-pipe flow issuing into a cold cross stream. *Phys. Fluids.* **26,** 3201-3210.

CARTER, C. D., DONBAR, J. M. & DRISCOLL, J. F. 1998 Simultaneous CH planar laser-induced fluorescence and particle imaging velocimetry in turbulent nonpremixed flames. *Appl. Phys. B.* **66,** 129-132.

DOLD, J. W. 1988 Flame propagation in a nonuniform mixture: the structure of anchored triple-flames. *Prog. Aero. Astro.* **113,** 240-248.

FRIC, T. F. & ROSHKO, A. 1994 Vortical structure in the wake of a transverse jet. *J. Fluid Mech.* **279,** 1-47.

HASSELBRINK, E. F. 1999 Transverse jets and jet flames: structure, scaling, and effects of heat release. *Ph.D. Thesis*, Stanford University.

HASSELBRINK, E. F., MUNGAL, M. G. & HANSON, R. K. 1997 Planar velocity measurements and OH imaging in a transverse jet flame. *AIAA Paper No. 97-0118.*

MÜLLER, C. M., BREITBACH, H. & PETERS, N. 1994 Partially premixed turbulent flame propagation in jet flames, In *Proc. Twenty-Fifth Symp. (Intl) on Combustion.* 1099-1106.

MUÑIZ, L. & MUNGAL, M. G. Instantaneous flame-stabilization velocities in lifted-jet diffusion flames Comb. Flame. *111.* **16-31.**

PETERS, N. & WILLIAMS, F. 1983 Liftoff characteristics of turbulent jet diffusion flames. *AIAA J.* **21,** 423–429.

REHM, J. E. & CLEMENS, N. T. 1997 A PLIF/PIV investigation of turbulent diffusion flames. *AIAA Paper No. 97-0250.*

SCHLÜTER, J. O., ANGELBERGER, C., SCHÖNFELD, T. & POINSOT, T. 1999 LES of jets in crossflow and its application to gas turbine burners, In *Proc. First Intl Symp. on Turbulence and Shear Flow Phenomena.* 71-76.

SMITH, S. H. & MUNGAL, M. G. 1998 Mixing, structure and scaling of the jet in crossflow. *J. Fluid Mech.* **357,** 83-122.

SU, L. K. & DAHM, W. J. A. 1996 Scalar imaging velocimetry measurements of the velocity gradient tensor field in turbulent flows. II. Experimental results. *Phys. Fluids.* **8,** 1883-1906.

Su, L. K., Han, D., Miraflor, R. M. & Mungal, M. G. 2000 Measurements of scalar and velocity fields in turbulent crossflowing jets with low velocity ratio. *AIAA Paper No. 2000-0815.*

Thurber, M. C. 1999 Acetone laser-induced fluorescence for temperature and multiparameter imaging in gaseous flows. *Ph.D. Thesis*, Stanford University.

Tsurikov, M. S., Rehm, J. E. & Clemens, N. T. 1999 High-resolution PIV/ PLIF measurements of a gas-phase turbulent jet. *AIAA Paper No. 99-0930.*

Watson, K. A., Lyons, K. M., Donbar, J. M. & Carter, C. D. 1999 Scalar and velocity field measurements in a lifted $CH_4$-air diffusion flame. *Comb. Flame.* **117,** 257-271.

Yuan, L. L. 1997 Large eddy simulations of a jet in crossflow. *Ph.D. Thesis*, Stanford University.